PIBB 生物化学与生物物理进展
Progress in Biochemistry and Biophysics
2020,47(10):1097~1108
www.pibb.ac.cn

Projection Area Evaluation of Macular Edema by Optical Coherence Tomography Images With Automatic Retinal Segmentation*

ZHANG Zhang**, TANG Yan-Hong**, ZENG Xing-Hui, XIONG Hong-Lian***, ZENG Ya-Guang***, HAN Ding-An***

(*School of Physics and Optoelectronic Engineering, Foshan University, Foshan* 528000, China)

Abstract In this paper, we propose an automatic retinal segmentation method to evaluate the projection area of macular edema (ME) on specific layers of the retina in optical coherence tomography (OCT) images. Ten retinal layer boundaries are segmented using an optimized Shortest-Path Faster Algorithm based on weight matrices first, which effectively reduces the algorithm's sensitivity to vascular shadows. However, the presence of ME will result in an inaccurate segmentation of the edema area. Therefore, we use the intensity threshold method to extract the edematous area in each OCT image, set the values in this area to zero, and ensure that the obtained segmented boundary can automatically cross rather than bypass the edematous area. We use the minimum projection method to calculate the projected area of ME at different layers. To test our method, we used data collected from Topcon's OCT machine. The measured macular area resolution in the axial and B-scan directions was 11.7 microns and 46.8 microns, respectively. The mean absolute and standard deviation difference values of the retinal layer boundary segmentations were 4.5±3.2 microns compared to manual segmentation. The proposed method, thus, provides an automatic, noninvasive, and quantitative tool for the evaluation of edema.

Key words optical coherence tomography, macular edema, retinal segmentation, projection area evaluation
DOI: 10.16476/j.pibb.2020.0071

Macular edema (ME) is the most common pathological outcome of many retinal diseases, such as diabetes, age-related macular degeneration, and retinal vein occlusion[1]. The pathogenesis of ME is closely related to blood vessels, which leak or exude fluids and blood when fragile blood vessels grow abnormally[2]. ME is a significant cause of vision loss and blindness[3]. Therefore, new and better methods to identify and characterize ME are essential for better disease diagnosis and surgical treatment.

Traditional fundus cameras can only provide two-dimensional images of the fundus[4]. ME usually occurs inside the retina, and it is thus difficult to observe and evaluate abnormalities through fundus photos. Optical coherence tomography (OCT) has been extensively used in ophthalmic diagnoses and is characterized by its increased detection sensitivity, high resolution, and noninvasiveness[5]. Recently, OCT is also used to monitor microvascular flow and thrombosis progression[6-7]. As shown in Figure 1, in this paper, we adopt the nomenclature established in the literature for retinal layers[8-9]. OCT images can provide ten structured layers of the retina, *i. e.*, the

* This work was supported by grants from the National Natural Science Foundation of China (61605026, 61771139, 81601534, 61705036, and 61805038), Natural Science Foundation of Guangdong Province (2017A030313386), High-level Construction and Scientific Research Project of Foshan University (CGG07141), and the High-level Talent Scientific Research Startup Project of Foshan University (gg040988).

** These authors contributed equally to this work.
*** Corresponding author.
Tel: 86-757-82716895
XIONG Hong-Lian. E-mail: yuanxiufeng138@163.com
ZENG Ya-Guang. E-mail: zeng.yg@163.com
HAN Ding-An. E-mail: handingan@163.com

Received: March 17, 2020 Accepted: June 16, 2020

nerve fiber layer (NFL), ganglion cell layer (GCL), inner plexiform layer (IPL), inner nuclear layer (INL), outer plexiform layer (OPL), outer nuclear layer (ONL), inner segment (IS), connecting cilia (CC), outer segment (OS), and the retinal pigment epithelium (RPE) layers. OCT images have been extensively used to diagnose macular disease[10]. By segmenting and projecting the layer structure of the retinal OCT images, we can obtain images of the blood vessels of different layers, which is important to assess the states of deep layers in ME.

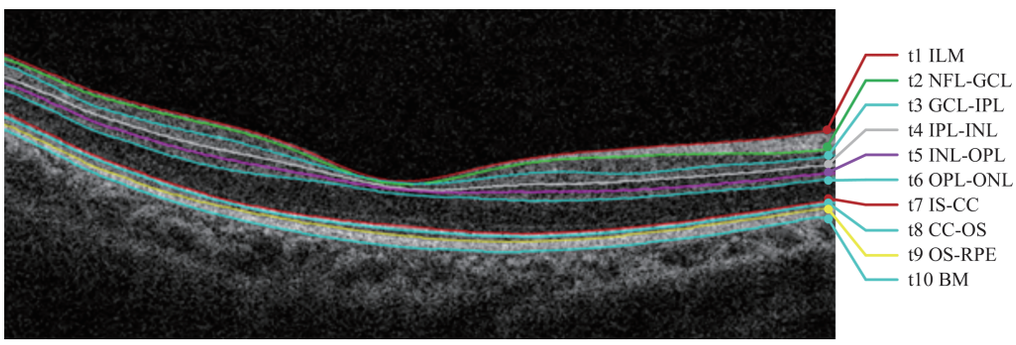

Fig. 1 Overview of the 10 retinal layer boundaries and their corresponding anatomical names

From top to bottom: inner limiting membrane (ILM), nerve fiber layer (NFL), ganglion cell layer (GCL), inner plexiform layer (IPL), inner nuclear layer (INL), outer plexiform layer (OPL), outer nuclear layer (ONL), inner segment (IS), connecting cilia (CC), outer segment (OS), and retinal pigment epithelium (RPE), and Bruch's membrane (BM).

The OCT system can achieve lateral and axial resolutions of the order of a few microns[11]. Given that the optical scattering of ME is smaller than the surrounding retinal tissue, it exhibits a distinct low-intensity characteristic in the OCT image. Detection and segmentation of edema from OCT volume has received considerable interest of researchers in recent years. There are also many research methods in the literature, such as the traditional image thresholding method[12], random forest classifier[13], and adversarial learning[14]. These methods achieve automatic segmentation of ME based on the different characteristics of the edema and normal areas. However, while these studies have focused on edema, they have not correlated edema with the specific layer structures of retinal lesions. To complete the visualization and projection area evaluation of ME in a specific layer of the retina, an accurate segmentation of the ME image is required. In recent decades, several categories of retinal layer segmentation methods have been developed to achieve quantification of the retinal layer structure, such as graph-based methods[8,15-16], machine- learning-based methods[17-19], combination of machine learning and graph theory methods[20-22], and others[23-26]. However, these segmentation methods relate to graph search methods and have certain limitations, that is, most of them are designed for normal retinal images. The fact that the presence of ME leads to the fusion of retinal layers, and the fact that the other layers are squeezed, the segmentation outcomes using these methods are not very satisfactory. When blood vessel shadows and edema are encountered in the case of the current graph search method, they are usually segmented along the edge of the edema because the intensity of the ME region tends to zero. To evaluate the projection area of ME, it is important to extract a segmentation line that can automatically directly cross the edematous region.

In this study, we developed an automatic retinal segmentation method to evaluate the projection area of ME in OCT images. Unlike the previous method that segmented and quantified edema directly from the B-scan image[12], our method attempts to visualize and evaluate ME using the projected images from different layers. This method uses a two-stage strategy. In the first step, we developed an optimized Shortest-Path Faster Algorithm (SPFA) to achieve segmentation of the ten retinal layer boundaries in which we defined the weight function by assigning different proportions of weights in both directions according to the lateral and longitudinal features in

order to reduce the effects of blood vessel shadows. In the second step, we used a threshold method to detect ME and used an interpolation scheme to force the dividing line to automatically cross the edema to achieve accurate layer segmentation of the ME area. Thus, retinal structures are accurately projected, and the lesion areas are calculated on the projection map. We validated the segmentation method on normal and ME OCT images and demonstrated the feasibility of the method as well.

1 Materials and methods

1.1 Image samples

All participants gave their informed consent for use of the acquired images samples in this study. Experimental data for four normal human eyes and six ME eyes were captured *via* a fundus tomography system (Topcon 3D OCT-1) in three-dimensional (3D) wide-capture mode. The scanned regions covered a 6 mm × 6 mm area centered on the macular and had a depth of 2 mm. Each volume contained 128 B-scans, and each B-scan contained 512 A-scans with 885 pixels per A-scan (512×128×885, corresponding to the *x*- , *y*- , and *z*-directions in the 3D coordinate system). To enhance the convenience of data processing, we adjusted every B-scan from 512×885 to 1 024×784 in the study.

1.2 Image preprocessing

Speckle noise caused by the limited spatial frequency bandwidth of the interference signal measured in OCT can greatly interfere and affect the contrast of the image, and it may thus cause segmentation errors. To this end, we used an adaptive-weighted bilateral filtering[27], which has proven effective in smoothing the OCT image and maintaining the texture information of the retinal layer. Figures 2a and 2b are the original images from the nonfoveal and foveal regions, respectively. The effects of filtering on the images without foveal areas are shown in Figure 2c. Accordingly, the filtering effects on the images with foveal areas are shown in Figure 2d.

To reduce the sensitivity of the algorithm to the direction and curvature of the retina and reduce the error caused by the obvious bending of the boundary, we utilized a retinal flattening algorithm[28] to flatten the retina. Figures 2e and 2f demonstrate that the retina is flattened in the center of the image based on the Bruch's membrane (BM) boundary, whereby Figure 2f is the flattened version of the filtered image (Figure 2e).

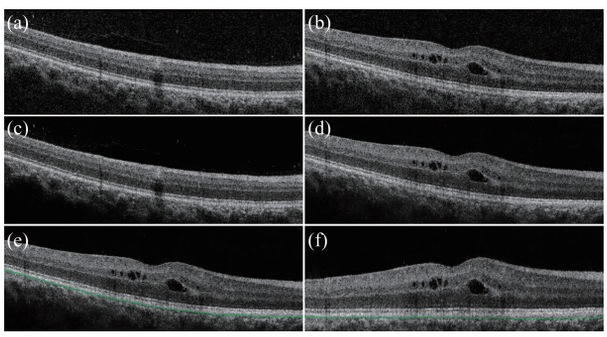

Fig. 2 Preprocessing steps

(a) and (b) are the original images from the nonfoveal and foveal regions, respectively, while (c) and (d) are filtered images. (e) and (f) denote the flattening process, whereby the green line is the baseline BM used for flattening.

1.3 Retinal layer segmentation

The purpose of this step is to initially segment the retinal layers for the subsequent ME lesion area determination procedure. The graph theory and dynamic programming (GHDP) -based segmentation framework has been proven to be effective for segmenting layered structures[8]. In the GHDP method, each pixel in the b-scan is regarded as a node, and each b-scan is regarded as a node graph; then the weight between the nodes is set according to the vertical gradient. Finally, the Dijkstra algorithm is used to find the shortest path in the node graph. We adopted its framework and proposed an improved graph search algorithm, which has two main improvements: a. the vertical gradient information is enhanced, and a weighting scheme of vertical gradient and lateral constraints in the calculation of weights is proposed; b. we adopted an optimized SPFA. The components of our segmentation algorithm are described in the following sections

1.3.1 Construction of weight matrix

We consider each pixel in an image as a node, and each image as a node graph. The connections of adjacent nodes in the graph are called weight edges. Assigning weights between nodes is crucial for the identification of the shortest path. The presence of blood vessels can cause shadows, and shadows pose a challenge to the segmentation process. When only

vertical features are used for segmentation, the boundaries may not be found correctly. Therefore, the lateral constraint was added. According to the flattened image, there were minor differences between the coordinate values in the *z*-direction. Therefore, we combined the gradient change value and the *z*-direction coordinate change value to define the weight function. The weight function between nodes *a* and *b* is defined by the following equation:

$$W_{ab} = 0.8 \times (G_a + G_b) + 0.2 \times S_{ab} + \mathrm{W}_{\min} \quad (1)$$

where W_{ab} is the weight assigned to the edge connecting nodes *a* and *b*; G_a and G_b are the vertical gradients of the image at nodes *a* and *b*, respectively; S_{ab} is the difference value between nodes *a* and *b* in the *z*-direction; and $\mathrm{W}_{\min}$ is the minimum weight of 10^{-5} in the graph added for system stabilization.

The acquisition of the gradient map is very important for defining the weight matrices. First, a Gaussian filter was performed on the flattened B-scan and a threshold was set to enhance the contrast between the light and dark layers. The B-scan was then normalized to ensure that the pixel intensity was between zero and one. Finally, given that the change between the retinal layers exhibited two transitional forms (dark-to-light and light-to-dark), a gradient calculation method [16] was used to generate two gradient maps, and a gamma transformation was used to enhance the gradient map. The two gradient maps were substituted into Eq. (1) to obtain two different weight matrices. The final gradient maps can be observed in Figure 3a and 3b.

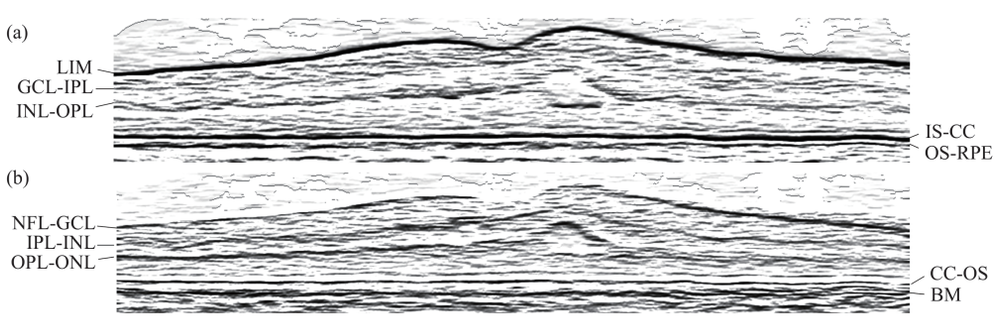

Fig. 3 Two gradient maps used for constructing different weight matrices

(a) Dark-to-light gradient map used to construct the weight matrix of ILM, GCL-IPL, INL-OPL, IS-CC, and OS-RPE. (b) Light-to-dark gradient map used to construct the weight matrix of NFL-GCL, IPL-INL, OPL-ONL, CC-OS, and BM.

1.3.2 Optimized SPFA method

To identify the layer boundaries within a short time period, SPFA and small label first (SLF) and large label last (LLL) were chosen as our graph search solution.

The combination of SPFA + SLF + LLL is an optimized solution. It can reduce the number of operations and can improve the accuracy of the path selection. We found the shortest path by searching only for five neighboring nodes for each node. The algorithm steps used for searching the shortest path were as follows:

Step 1. Set the first-in first-out queue to save the nodes that need to be optimized.

Step 2. Take out the first node (corresponding to the upper left node of the image) from the queue and release the next node.

Step 3. If the total weight value of the new node is less than the total weight of the current queue head node and less than the average value of the weight matrix, the new node is added to the head of the queue; otherwise it is placed at the end of the queue.

Step 4. Repeat steps 2 and 3 until the queue is empty.

1.3.3 Automatic segmentation of the ten boundaries

Before the subsequent iterative segmentation, we need to preliminarily segment the ILM and IS-CC to construct the region-of-interest (ROI) and then iteratively update all boundaries based on the selected ROI.

Both ILM and IS-CC are highly reflective layers with the most obvious gradient changes. They constitute the two most prominent layer boundaries in the retinal image. Given that they exhibit dark-to-bright transition forms, the dark-to-bright weight matrix obtained in Section **1.3.1** was used in

conjunction with the optimized SPFA introduced in Section **1.3.2** to obtain approximate segmentations of the ILM and IS-CC layer boundaries. Finally, the average value of the row in the z-direction was calculated according to the layer boundary identified after two iterations. The smaller value corresponds to ILM. The initial ILM and IS-CC segmentation outcomes are shown in Figure 4.

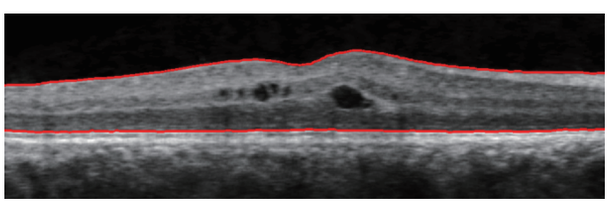

Fig. 4　Initial segmentation outcomes of ILM and IS−CC

To prevent the algorithm from accidentally dividing extraneous structures into target features, the image was restricted to an effective search region, that is, the ROI, thereby eliminating the influence of irrelevant factors and improving the quality and efficiency of the segmentation. The segmentation needs to adhere to a predetermined order (Figure 5) to minimize segmentation errors. First, we defined the ROI near the ILM and IS-CC, which was used to update ILM and IS-CC. We then defined an ROI below the updated IS-CC boundary to allow the identification of the BM boundary. Finally, the remaining boundaries are based on these boundaries in order to determine the ROI, and the shortest path is determined based on the optimized SPFA. As it can be observed from the section on the construction of the weight matrix that ILM, GCL-IPL, INL-OPL, IS-CC, and OS-RPE change from dark-to-light, and NFL-GCL, IPL-INL, OPL- ONL, CC-OS, and BM change from light-to-dark. Different changes require different weight matrices to be used, and the desired retinal layer is then segmented. A total of ten iterations can segment ten boundaries.

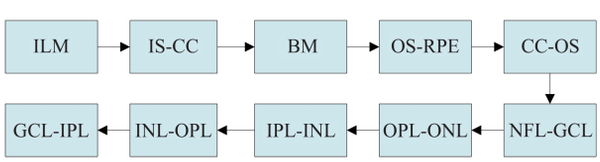

Fig. 5　Segment order of the retinal layer boundaries

1.4　ME lesion area determination

The purpose of this step is to refine the segmentation results based on detection of edema and achieve the structural projection of layers and calculation of the ME areas in the projection map.

1.4.1　Edema detection

Figure 6 shows the main steps of edema detection, which are described in detail in the following sections.

To simplify the edema detection process, it is important to set the ROI at a proper position. We first employed an adaptive bilateral filtering (introduced in Section **1.2**) with larger parameter values on the flattened retinal image. We then limited the detected area with the retinal mask, maintained the pixel values of the pixels inside the retinal mask, and set the pixel values of those pixels outside of the retinal mask to zero, which helped us eliminate interferences outside of the retinal region. The resulting ROI of the detected edema is shown in Figure 6a.

Second, the probabilities of the edematous regions were defined by the pixels whose intensity values were below the empirical value of 20. The empirical value of 20 was set according to the robust average value "IA" and some additional tests. Accordingly, the robust average value "IA" was 10% larger than the average pixel intensity of the edema ROIs, which were manually segmented *a priori*. We used a binary image in Figure 6b to show the probability image of the edematous regions, whereby the white pixels with unity values represent the edematous regions and the black pixels with zero values represent the background.

Third, the total area of the edematous regions was set to a value larger than 100 pixels. In this way, the regions that do not meet the criteria should be removed, as shown in Figure 6c. We set 100 as the threshold because we found that the edematous areas that affected the segmentation accuracy were generally larger than 100 pixels. Furthermore, the probability regions with smaller areas may not be edema regions.

In the last step of edema detection, we applied some morphological operations, such as dilatation and erosion to the probability images. The dilatation step filled the inner holes and the edges of the probability

regions, while the erosion step shrunk the edge to yield accurate edema regions. The result after dilatation erosion is shown in Figure 6d.

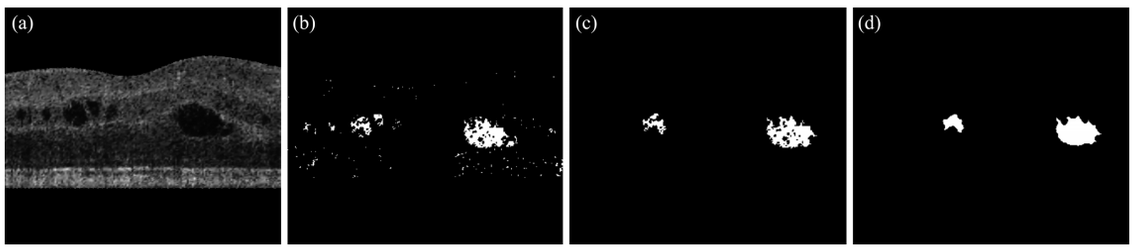

Fig. 6 Edema detection steps

All subfigures are from the same B-scan with edematous regions. (a) Region-of-interest (ROI) for edema detection. (b) Probability edema regions. (c) Threshold processing. (d) Morphological operation.

1.4.2 Boundary correction and optimization of ME images

Because edematous regions with large areas introduce serious errors in the automatic segmentation process, we corrected the segmentations of those areas that were affected by edema based on the edematous regions detected in Section **1.4.1**. We first found the exact locations (rows and columns) of ME and then blocked the edematous regions and replaced them with one-dimensional linearly interpolated outcomes so that the dividing line can directly cross the edema to achieve automatic correction of the retinal layer boundaries of the ME areas.

After the correction of all the layer boundaries in the ME images, we also needed to perform smoothing and optimization operations on the segmentation line. First, we used cubic spline interpolation method to smooth 10 curves for each B-scan, which was closer to the true curve compared to the quadratic curve fitting method. Second, for the 128-frame image of the same volume, we utilized the fact that continuity existed between the frames and used a median filter (filter kernel: 1×7) for each curve. This method can correct obvious segmentation errors in B-scans. Finally, after optimizing all the curves, we unflattened the image by moving pixels upward or downward—in the direction opposite to that of the image flattening direction to restore the original curvature.

1.4.3 Structural projection and lesion area calculation

After the segmentation, a structural projection method was employed on the segmented volume to visualize the vascular structure of each layer of the retina. Structural projection techniques are designed to allow the observation of the position and state of the lesion area in a more intuitive manner and to assist in the subsequent calculation of the lesion area. Specifically, a minimum projection method was proposed that tracked the grayscale features in the image based on the calculation of the minimum pixel value on every A-scan given that the interest in this study were the ME regions with low-intensity values. Hence, the final structural projection map encompassed the largest area of the lesion area. We projected the 3D binary ME OCT volume (the binary ME images obtained using the edema detection step in Section **1.4.1**, but the area threshold was modified from 100 to 20) with the projection technique to display the lesion area and calculated the lesion area within the entire 6 mm×6 mm projection map.

2 Results and discussion

Compared with the previous technique of edema segmentation in every B-scan and the quantification of the total volume occupied by ME from OCT image volume [12], our algorithm provided a new idea for evaluating the area of edema on the projection map. Experimental results show that our algorithm is feasible. The proposed algorithm was implemented in MATLAB. We executed the algorithm on a desktop that was equipped with an Inter(R) Core (TM) i7-7700 central processing unit @3.60 GHz and 16 GB random access memory.

For retinal layer segmentation, we tested our algorithm on normal and ME eyes (Table 1). The ten layers were segmented in all the OCT images to

identify ILM, NFL-GCL, GCL-IPL, IPL-INL, INL-OPL, OPL-ONL, IS-CC, CC-OS, OS-RPE, and BM.

Table 1　Tested optical coherence tomography （OCT） volumetric data

Scan range	6 mm×6 mm	
Diagnosis	Healthy	Macular edema
Eyes	4	6
Volumetric scans	4	6

The method efficacy is verified based on layer segmentation experiments on normal and ME images. The average running time of each image was 10 s (784×1024 pixels and all images were segmented to include 10 boundaries). Figure 7 is a representative segmentation result obtained by our algorithm to segment ten retinal layer boundaries on normal adult eyes, whereby Figures 7a and 7f are B-scans of the nonfoveal and foveal areas, respectively. Figure 7c−e show detailed blocks extracted from the segmented B-scan (Figure 7b). As it can be observed from Figure 7c – e and 7h, our method can correctly segment the retinal layer boundaries, even in the shadow area of the blood vessel (Figure 7c−e) and the foveal area (Figure 7h). Figure 8 shows the segmentation results of our algorithm after its application to the segmentation of ME eyes. As it can be observed from Figure 8, our method achieved the expected results given that the dividing line can cross the edematous region. The IPL, INL, and OPL layers are the main locations of the edema. Accordingly, they are the main target layers based on which we evaluate the area of ME in the projection map.

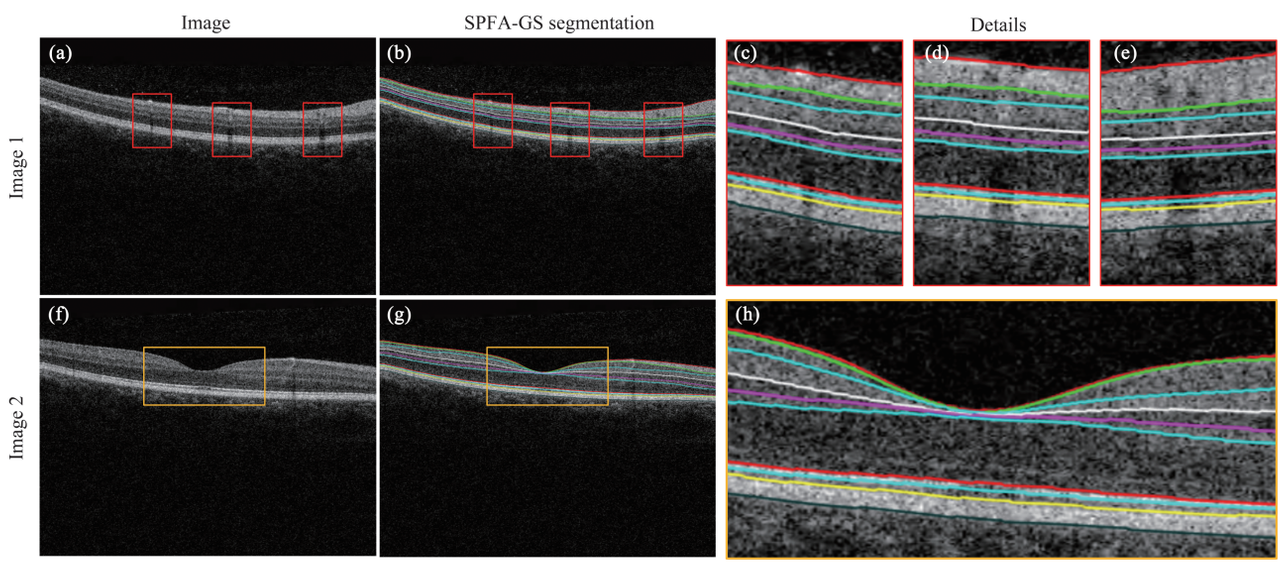

Fig. 7　Segmentation results of normal eyes

(Top row) (a) Nonfoveal B-scan of three-dimensional (3D)-OCT volume, (b) automatic segmentation of (a) using the optimized shortest path fastest algorithm and graph search (SPFA-GS) for all the 10 retinal layer boundaries, and (c−e) detailed block extracted from (b). (Bottom row) (f) Foveal B-scan, (g) its segmentation, and (h) detailed block outcome.

To evaluate the performance of our retinal layer segmentation method in more detail, we compared our method with the GHDP method proposed by Chiu *et al.*[8] on healthy and ME images. For the healthy case, we randomly selected 4 B-scans including the fovea from each volume scan, for a total of 16 B-scans. For ME case, we randomly selected 4 B-scans around the fovea from each volume scan, for a total of 24 B-scans. For all B-scans, we calculated the mean absolute error and standard deviation of each boundary between the smooth, manually segmented results and the automatically segmented results, and then averaged to obtain the overall difference. The comparison outcomes of the two methods are listed in Table 2. As indicated, our segmentation method demonstrated an overall mean absolute error and standard deviation of 1.75±1.25 pixels (4.5±3.2 microns), respectively, compared to manual

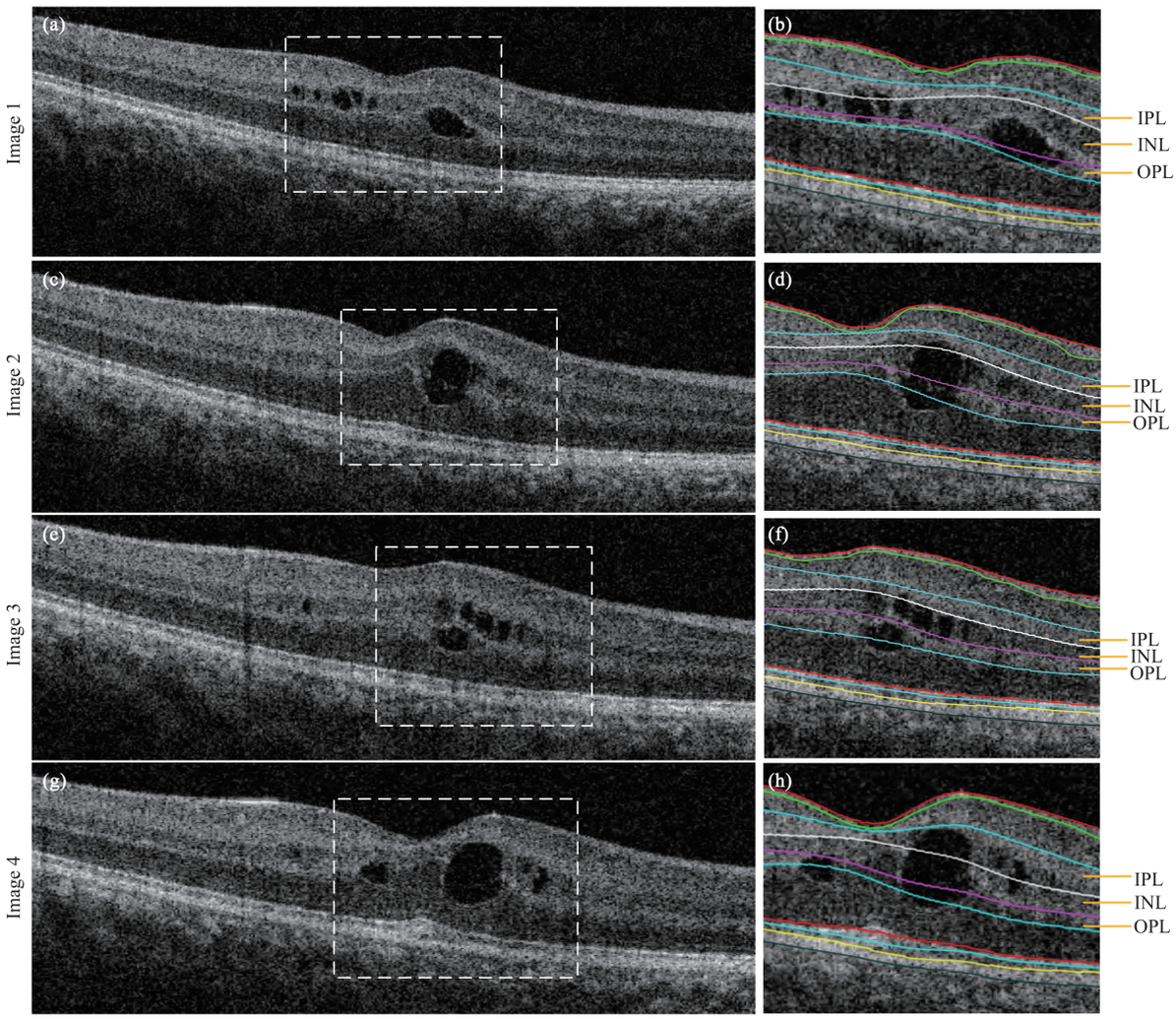

Fig. 8 ME eye segmentation outcomes

(a), (c), (e), (f): Four B-scans from different locations of the same OCT volume scan. (b), (d), (f), (h): automatic segmentation outcomes in which the IPL, INL, and OPL layers are the main locations of edema.

Table 2 Comparison of performance between manual and automatic segmentation for healthy and ME cases

Boundaries	Chiu *et al*. [8] (Healthy)	Chiu *et al*. [8] (ME)	Our method (Healthy)	Our method (ME)
ILM	0.75±0.67	1.08±1.21	0.77±0.54	0.84±0.58
NFL-GCL	1.89±1.99	5.32±6.67	1.58±1.15	1.51±1.12
GCL-IPL	—	—	2.47±1.68	3.42±2.32
IPL-INL	2.75±2.49	4.35±3.76	3.33±2.06	2.87±2.03
INL-OPL	2.0±1.83	2.13±2.13	2.18±1.51	1.95±1.54
OPL-ONL	1.33±1.34	3.33±3.26	1.81±1.39	2.63±2.28
IS-CC	1.56±1.47	1.75±1.71	1.17±0.81	1.14±0.77
CC-OS	—	—	0.85±0.60	1.06±0.71
OS-RPE	—	—	1.28±0.91	1.62±1.13
BM	1.88±1.79	1.70±1.81	0.95±0.69	1.6±1.08
Overall	1.73±1.65	2.76±2.65	1.64±1.13	1.86±1.36

Differences were measured in pixels and expressed as mean absolute ± standard deviation values.

segmentation. The results show that the similarity of our method with manual segmentation is higher than with others.

In conclusion, accurate layer boundary segmentation is an important tool for the evaluation of retinal diseases. However, the presence of ME poses a great challenge to the segmentation of the retina. Accurate segmentation enables the characterization and evaluation of ME in a single retinal layer. Compared with the segmentation algorithm based on vertical gradient and additional vessel detection [8], our method considered two directional constraint conditions based on which it could effectively solve vessel shadow problems. Additionally, we corrected the boundaries based on detection of edema, and the smooth constraint of consecutive B-scans helped improve segmentation accuracy.

For the determination of the ME lesion area, detection of edema in important in two ways: The presence of edema can lead to fusion between the retinal layers, thereby making the boundaries of the layers unclear and introducing challenges in the retinal layer segmentation process. The detection of edema can identify the edema that has a great impact on the segmentation so as to correct the segmentation error caused by large edematous regions. Conversely, projection area evaluation of ME also depends on the detection of edema. Projecting a binary map of a detected edematous region helps accurately calculate the edematous area on the projection map.

We selected a segmented 3D OCT image from a patient with ME and extracted the three representative layers (IPL, INL, and OPL), to achieve a minimum projection. It can be observed from the projection effect (Figure 9a−c) that ME has different degrees of influence on the three layers of the retina—with the INL layer being affected the most by ME. Results show that application of the minimum projection technique on the segmented retinal volume can allow a more intuitive observation of the location and status of ME. To calculate the ME projection area, we projected the 3D binary ME B-scans to identify lesions (red parts in Figure 9d−f) and then calculated the lesion areas based on the formula: area = 6×6×(Ne/NI), where Ne denotes the pixels in the edema area and NI is the total number pixels in the entire image. The calculated areas are 0.20 mm^2, 0.96 mm^2, and 0.45 mm^2, respectively.

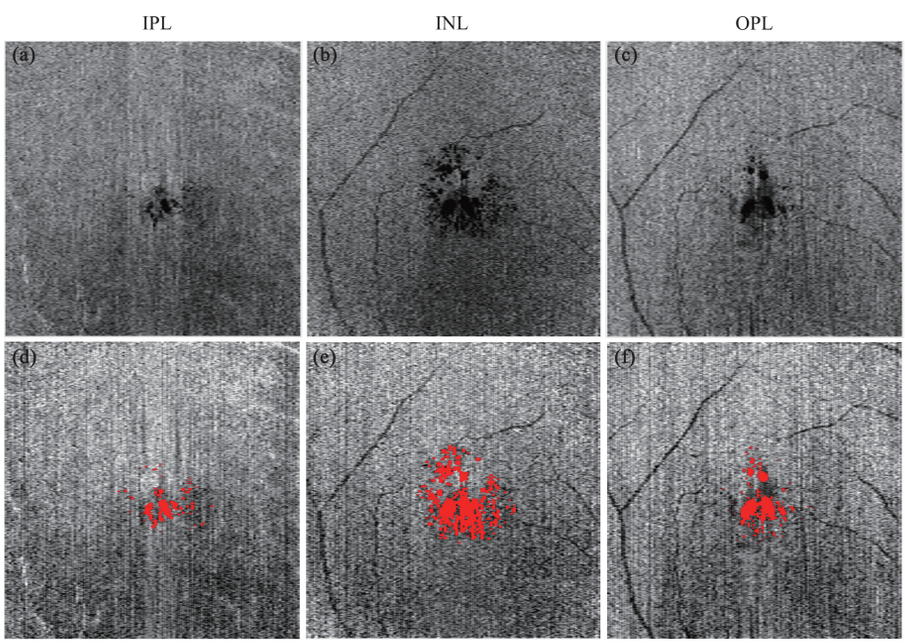

Fig. 9　Minimum projection

(a−c): from left to right are the projection effects of IPL, INL, and OPL. (d−f): The parts shown in red are lesion areas corresponding to (a−c), and the areas of the lesions are 0.20 mm^2, 0.96 mm^2, and 0.45 mm^2, respectively.

According to experimental results, our method can successfully evaluate the projection area of ME in the special layers. This is achieved *via* the two steps of retinal layer segmentation and ME lesion area determination. An accurate segmentation of ME images is a prerequisite for the determination of the lesion areas. Our retinal segmentation method can segment the healthy and diseased retinas, including the hyporeflexia areas that were affected by ME and vascular shadows. In manual segmentation, some boundaries cannot be determined quickly and/or accurately owing to image problems, but the algorithm can automatically segment layer boundaries according to the gradient and location information. Recently, deep learning methods have gained wider use in the segmentation of retinal layers and pathological structures and have achieved high-quality results[29-31]. An advantage of our method is that it does not require model training and can quickly identify relatively accurate layer boundaries based on image features and optimized SPFA. Moreover, we proposed an idea for edema evaluation based on projection maps. By determining the severity of the deep layer's ME, physicians can obtain better diagnoses and treatment of eye diseases.

Even though the experimental results show that the proposed method can achieve higher layer boundary segmentation accuracies and can constitute an efficient clinical tool for the evaluation of lesion areas, there are certain limitations, which are summarized as follows. First, the retinal layer segmentation method depends strongly on the gradient information at the layer boundaries and may fail in cases of severe structural deformations caused by other retinopathy (such as macular holes). Second, to observe the lesion area on the projection map, we adjusted the projection map matrix size from 512×128 to 512×512 (corresponding to the xy plane) based on interpolation. Nevertheless, the actual resolutions of the pixels in the *x*- and *y*-directions are 11.7 microns and 46.8 microns, respectively, which can cause finite errors in the *y*-direction of the ME projection area. This can be improved by changing the acquisition method. Third, methods for automatic setting of the threshold for detection of edema have not been proposed yet. If the threshold is set to be too large, it will contain non-ME shaded areas. If the threshold is set to be too low, some small edematous areas will be missed.

3 Conclusion

In this study, a retinal layer segmentation-based ME projection area evaluation algorithm was proposed to calculate the ME areas in the projection maps. We proposed an automatic retinal segmentation method based on optimized SPFA to identify ten retinal layer boundaries in OCT images, and introduced a lesion detection algorithm based on binary masks, morphological methods, and structural projection. Our algorithm yielded acceptable segmentation accuracies in normal and ME images. In future publications, we will incorporate machine learning to the proposed optimized SPFA method to flexibly divide the ROI and reduce errors based on the use of prior knowledge. In addition, we plan to use our method to other retinopathies (*e. g.*, age-related macular degeneration, diabetic retinopathy, glaucoma, and others).

References

[1] Tranos P G, Wickremasinghe S S, Stangos N T, *et al*. Macular edema. Survey of Ophthalmology, 2004, **49**(5): 470-490

[2] Antcliff R, Marshall J. The pathogenesis of edema in diabetic maculopathy. Seminars in Ophthalmology, 1999, **14**(4): 223-232

[3] Bhagat N, Grigorian R A, Tutela A, *et al*. Diabetic macular edema: pathogenesis and treatment. Survey of Ophthalmology, 2009, **54**(1): 1-32

[4] Abràmoff M D, Garvin M K, Sonka M. Retinal imaging and image analysis. IEEE Reviews in Biomedical Engineering, 2010, **3**: 169-208

[5] Huang D, Swanson E A, Lin C P, *et al*. Optical coherence tomography. Science, 1991, **254**(5035): 1178-1181

[6] Ma Z, Luo S, Yu M, *et al*. Assessment of microvasculature flow state with a high speed all-optic dual-modal system of optical coherence tomography and photoacoustic imaging. Biomedical Optics Express, 2018, **9**(12): 6103-6115

[7] Yu Y, Yu M, Liu J, *et al*. *In vivo* monitoring of thrombosis in mice by optical coherence tomography. Journal of Biophotonics, 2019, **12**(11): e201900105

[8] Chiu S J, Li X T, Nicholas P, *et al*. Automatic segmentation of seven retinal layers in SDOCT images congruent with expert manual segmentation. Optics Express, 2010, **18**(18): 19413-19428

[9] Rathke F, Schmidt S, Schnörr C. Probabilistic intra-retinal layer segmentation in 3-D OCT images using global shape regularization. Medical Image Analysis, 2014, **18**(5): 781-794

[10] Hee M R, Puliafito C A, Wong C, *et al*. Quantitative assessment of macular edema with optical coherence tomography. Archives of Ophthalmology, 1995, **113**(8): 1019-1029

[11] Drexler W, Fujimoto J G. Optical coherence tomography:

technology and applications. Berlin: Springer Science & Business Media, 2008

[12] Wilkins G R, Houghton O M, Oldenburg A L. Automated segmentation of intraretinal cystoid fluid in optical coherence tomography. IEEE Transactions on Biomedical Engineering, 2012, **59**(4): 1109-1114

[13] Lang A, Carass A, Swingle E K, *et al*. Automatic segmentation of microcystic macular edema in OCT. Biomedical Optics Express, 2015, **6**(1): 155-169

[14] Liu X, Cao J, Fu T, *et al*. Semi-supervised automatic segmentation of layer and fluid region in retinal optical coherence tomography images using adversarial learning. IEEE Access, 2018, **7**: 3046-3061

[15] Lang A, Carass A, Calabresi P A, *et al*. An adaptive grid for graph-based segmentation in retinal OCT //Medical Imaging 2014: Image Processing. Bellingham: International Society for Optics and Photonics, 2014: 903402

[16] Guo Y, Camino A, Zhang M, *et al*. Automated segmentation of retinal layer boundaries and capillary plexuses in wide-field optical coherence tomographic angiography. Biomedical Optics Express, 2018, **9**(9): 4429-4442

[17] Zawadzki R J, Fuller A R, Wiley D F, *et al*. Adaptation of a support vector machine algorithm for segmentation and visualization of retinal structures in volumetric optical coherence tomography data sets. Journal of Biomedical Optics, 2007, **12**(4): 041206

[18] Shah A, Zhou L, Abrámoff M D, *et al*. Multiple surface segmentation using convolution neural nets: application to retinal layer segmentation in OCT images. Biomedical Optics Express, 2018, **9**(9): 4509-4526

[19] Krizhevsky A, Sutskever I, Hinton G E. Imagenet classification with deep convolutional neural networks //Advances in neural information processing systems. New York: Curran Associates, 2012: 1097-1105

[20] Antony B J, Abràmoff M D, Harper M M, *et al*. A combined machine-learning and graph-based framework for the segmentation of retinal surfaces in SD-OCT volumes. Biomedical Optics Express, 2013, **4**(12): 2712-2728

[21] Kugelman J, Alonso-Caneiro D, Read S A, *et al*. Automatic segmentation of OCT retinal boundaries using recurrent neural networks and graph search. Biomedical Optics Express, 2018, **9**(11): 5759-5777

[22] Fang L, Cunefare D, Wang C, *et al*. Automatic segmentation of nine retinal layer boundaries in OCT images of non-exudative AMD patients using deep learning and graph search. Biomedical Optics Express, 2017, **8**(5): 2732-2744

[23] Gawlik K, Hausser F, Paul F, *et al*. Active contour method for ILM segmentation in ONH volume scans in retinal OCT. Biomedical Optics Express, 2018, **9**(12): 6497-6518

[24] Yazdanpanah A, Hamarneh G, Smith B, *et al*. Intra-retinal layer segmentation in optical coherence tomography using an active contour approach //International Conference on Medical Image Computing and Computer-Assisted Intervention. Berlin: Springer, 2009: 649-656

[25] Koozekanani D, Boyer K, Roberts C. Retinal thickness measurements from optical coherence tomography using a Markov boundary model. IEEE Transactions on Medical Imaging, 2001, **20**(9): 900-916

[26] De Sisternes L, Jonna G, Moss J, *et al*. Automated intraretinal segmentation of SD-OCT images in normal and age-related macular degeneration eyes. Biomedical Optics Express, 2017, **8**(3): 1926-1949

[27] Anantrasirichai N, Nicholson L, Morgan J E, *et al*. Adaptive-weighted bilateral filtering and other pre-processing techniques for optical coherence tomography. Computerized Medical Imaging and Graphics, 2014, **38**(6): 526-539

[28] Lang A, Carass A, Hauser M, *et al*. Retinal layer segmentation of macular OCT images using boundary classification. Biomedical Optics Express, 2013, **4**(7): 1133-1152

[29] Ruan Y, Xue J, Li T, *et al*. Multi-phase level set algorithm based on fully convolutional networks (FCN-MLS) for retinal layer segmentation in SD-OCT images with central serous chorioretinopathy (CSC). Biomedical Optics Express, 2019, **10**(8): 3987-4002

[30] He Y, Carass A, Liu Y, *et al*. Deep learning based topology guaranteed surface and MME segmentation of multiple sclerosis subjects from retinal OCT. Biomedical Optics Express, 2019, **10**(10): 5042-5058

[31] Chen A, Ong C Z L, Luo W, *et al*. Comparison of training strategies for the segmentation of retina layers in optical coherence tomography images of rodent eyes using convolutional neural networks //Medical Imaging 2020: Image Processing. Bellingham: International Society for Optics and Photonics, 2020: 1131339

通过光学相干断层扫描图像进行自动视网膜分割评估黄斑水肿的投影面积*

张 章** 唐艳红** 曾兴晖 熊红莲*** 曾亚光*** 韩定安***

（佛山科学技术学院物理与光电工程学院，佛山 528000）

摘要 本文提出一种自动视网膜分割方法，以评估光学相干断层扫描（OCT）图像中黄斑水肿（ME）在视网膜特定层上的投影面积. 首先使用基于权重矩阵的优化最短路径最快算法对10个视网膜层边界进行分割，这有效降低了算法对血管阴影的敏感性. 然而，ME的存在将导致水肿区域的分割不准确. 因此，使用强度阈值方法提取每个OCT图像中的水肿区域，并将该区域中的值设置为零，并确保获得的分割边界可以自动穿过而不是绕过水肿区域. 同时使用最小值投影来计算ME在不同层的投影面积. 为了测试该方法，使用了从Topcon OCT机器收集的数据. 在轴向和B扫描方向上测得的黄斑区域分辨率分别为11.7 μm和46.8 μm. 与手动分割相比，视网膜层边界分割的平均绝对误差和标准偏差为（4.5±3.2）μm. 因此，所提出的方法为评估水肿提供了一种自动、无创和定量的工具.

关键词 光学相干断层扫描，黄斑水肿，视网膜分割，投影面积评估

中图分类号 R445 **DOI**：10.16476/j.pibb.2020.0071

* 国家自然科学基金（61605026，61771139，81601534，61705036和61805038），广东省自然科学基金（2017A030313386），佛山科学技术学院高层次建设与科研项目（CGG07141）和佛山科学技术学院高层次人才科研启动项目（gg040988）资助.

** 并列第一作者.

*** 通讯联系人. Tel：0757-82716895

熊红莲. E-mail：yuanxiufeng138@163.com

曾亚光. E-mail：zeng.yg@163.com

韩定安. E-mail：handingan@163.com

收稿日期：2020-03-17，接受日期：2020-06-16